New Journal of Physics
The open-access journal for physics

Normal modes of trapped ions in the presence of anharmonic trap potentials

J P Home[1,2], **D Hanneke, J D Jost, D Leibfried and D J Wineland**
National Institute of Standards and Technology, 325 Broadway, Boulder,
CO 80305, USA
E-mail: jhome@phys.ethz.ch

New Journal of Physics **13** (2011) 073026 (25pp)
Received 25 May 2011
Published 20 July 2011
Online at http://www.njp.org/
doi:10.1088/1367-2630/13/7/073026

Abstract. We theoretically and experimentally examine the effects of anharmonic terms in the trapping potential for linear chains of trapped ions. We concentrate on two different effects that become significant at different levels of anharmonicity. The first is a modification of the oscillation frequencies and amplitudes of the ions' normal modes of vibration for multi-ion crystals, resulting from each ion experiencing a different curvature in the potential. In the second effect, which occurs with increased anharmonicity or higher excitation amplitude, amplitude-dependent shifts of the normal-mode frequencies become important. We evaluate normal-mode frequency and amplitude shifts, and comment on the implications for quantum information processing and quantum state engineering. Since the ratio of the anharmonic to harmonic terms typically increases as the ion–electrode distance decreases, anharmonic effects will become more significant as ion trap sizes are reduced. To avoid unwanted problems, anharmonicities should therefore be taken into account at the design stage of trap development.

---

[1] Current address: Institute of Quantum Electronics, ETH Zürich, Schafmattstrasse 16, 8093-Zürich, Switzerland.
[2] Author to whom any correspondence should be addressed.

Contents

1. Introduction **2**
2. Calculating normal modes of trapped ion chains **4**
  2.1. One-dimensional simplification . . . 5
3. Anharmonic modifications to normal modes **5**
  3.1. Illustrative examples . . . 5
  3.2. Experimental demonstrations . . . 8
  3.3. Frequency shifts, homogeneous ion crystals . . . 10
  3.4. Frequency shifts, inhomogeneous ion crystals . . . 11
  3.5. Nulling odd-order anharmonicities . . . 14
4. Strong anharmonic effects: modifications to the normal-mode picture **15**
  4.1. Perturbation theory . . . 15
  4.2. Example case: a microfabricated surface trap . . . 17
  4.3. Coherence during quantum state manipulations . . . 19
5. Sensitivity to electric fields **21**
6. Conclusion **22**
Acknowledgments **22**
References **22**

1. Introduction

Quantum control of the motional degrees of freedom of trapped atomic ions is among the most advanced in physics. It has an important role in realizing deterministic quantum information processing with trapped ions and offers a rich playground for the exploration of quantum-state engineering and quantum control. Examples of the latter include the production of Fock states, squeezed states, coherent states, and superpositions of coherent states analogous to the 'Schrödinger's cat' thought experiment [1–5]. The motional states of trapped ions have been a key ingredient for simulation of quantum-optical systems [6] and the Dirac equation [7, 8], and for the realization of quantum walks in phase space [9, 10].

For ion-trap quantum information processing [11], the collective motion of the ions is critical for performing deterministic multi-qubit quantum gates. Recent work includes the entanglement of up to 14 ions [12], and a two-qubit entangled state fidelity of 99.3% [13]. In order to perform more complex operations, higher precision control of both the internal and motional states of the ions will be required, and scalable techniques will need to be implemented [14]. The high operation fidelities of around 99.99% required to achieve fault-tolerance for quantum information processing [15, 16] place stringent demands on the motional control.

Most of the experimental work performed to date has used traps where the potential is harmonic to a very high degree. The resultant normal-mode frequencies and amplitudes have been studied extensively [17–19]. The relative importance of anharmonic terms depends primarily on their length scales relative to those relevant to the ions. In this paper, we consider two important effects that occur at different length scales. Firstly, weak anharmonicity modifies the normal modes of multi-ion chains when anharmonic terms become significant over the length L of a chain of ions. In this case the ions' equilibrium positions are modified and the local curvature of the potential is different at the position of each ion. This modifies both the frequency and ion amplitudes of the normal modes of the chain, but the normal-mode eigenstates are still stationary states of the Hamiltonian. Secondly, strong anharmonicity plays a role when changes in curvature over the size of the motional wavefunction become significant. This creates motional frequency shifts as a function of the motional excitation and cross-coupling between different normal modes. The effects of strong anharmonicity have been observed when caused by anharmonicity in the Coulomb interaction between the ions [20, 21]; we extend these results to include anharmonicity in the trapping potential. The Coulomb anharmonicity plays a crucial role in the prediction of a temperature-driven structural phase transition in ion chains [22, 23], and anharmonic trap potentials will modify the effect and perhaps allow it to be tuned. Although we focus in this paper on anharmonicity as a perturbation to harmonic trap potentials, several experiments use strongly anharmonic potentials to split and recombine chains of ions [14], [24–26] and to engineer ion chains with nearly equal ion spacing [27].

Manipulating ions in small-scale traps that can be microfabricated is useful for large-scale quantum information processing [14, 28, 29]; for achieving more intricate motional control [25], [30–33]; and for coupling trapped ions to other quantum devices [34–37]. Anharmonic terms have the potential to scale unfavorably as trap sizes are reduced. Consider a trap with some characteristic length scale ρ. This length might be, for example, the distance from a trapped ion to the nearest point on the surface of a trap electrode. In an expansion of the trap potential V_t, the size of the nth term is proportional to $\partial^n V_t/\partial z^n$ and thus it will tend to scale as ρ^{-n+2} relative to the harmonic term. Moreover, some recent microfabricated traps employ a geometry in which the ion resides above a surface containing the electrodes [29], [38–40]. The intrinsic asymmetry in these surface-electrode traps can lead to large odd-order anharmonicities in the direction perpendicular to the electrode surface. While anharmonicities should tend to increase with decreasing trap size, the trap potential can still be engineered to suppress them, provided the trap is designed with sufficient degrees of freedom.

To give a sense of the typical lengths involved, we note that a single $^9\text{Be}^+$ ion in the ground state of a 1 MHz harmonic potential has a root-mean-square wavefunction size of $\sigma = 24\,\text{nm}$. Two ions in the same potential are separated by $L = 9\,\mu\text{m}$. Recent trends in quantum information are towards increased numbers of ions to perform multi-qubit operations simultaneously on many qubits [12], [41–44], to accommodate sympathetic refrigerator ions along with those used to store qubits [14], [25–27], and to encode logical qubits in multiple physical qubits [45–47]. For chains containing eight ions, trap frequencies along the chain direction between 1 and 5 MHz lead to a range of L between 36 and 12 μm.

The paper is organized as follows. After a brief introduction to calculation methods for normal modes of trapped-ion crystals, we discuss weak anharmonicities, giving simple examples, experimental results, and methods for characterization. Next, we theoretically treat effects arising from stronger anharmonicities. We evaluate these effects with reference to a surface-electrode trap that has been used at NIST. In both sections, we discuss the implications of our results for precise control of trapped-ion chains for quantum information and state-engineering, focusing on multi-qubit quantum logic gates that use the ions' normal modes. Finally, we provide a short discussion of the susceptibility of anharmonic traps to electric field drift, after which we conclude.

2. Calculating normal modes of trapped ion chains

Normal-mode frequencies and amplitudes may be calculated from the classical Lagrangian equations of motion and quantized with the usual harmonic-oscillator algebraic formalism. We consider the case of N ions each with charge q in a potential well. The energy of the ions is given as a sum of kinetic- and potential-energy terms $E = T + U$, where

$$\begin{aligned} T &= \sum_{i=1}^{N} \frac{m_i}{2} \dot{z}_i^2, \\ U &= \sum_{i=1}^{N} q V_t(\mathbf{z}_i, m_i) + \frac{1}{2} \sum_{\substack{j,i=1 \\ j \neq i}}^{N} \frac{q^2}{4\pi\epsilon_0 |\mathbf{z}_i - \mathbf{z}_j|}. \end{aligned} \tag{1}$$

Here m_i, $\mathbf{z}_i$ denote the mass and position of the ith ion. The trap potential V_t includes both a mass-independent static potential and a mass-dependent pseudopotential arising from the radiofrequency confinement [35]. In what follows, it is convenient to write the coordinates as $3N$ scalar parameters $z_1, \ldots, z_{3N}$ that produce the N vectors $\mathbf{z}_1, \ldots, \mathbf{z}_N$.

The set of equations $\partial U / \partial z_i = 0$ give the set of equilibrium positions $\{z_i^0\}$ for the ions. For large N this is done by numerical minimization, since the analytical expressions become complicated. In a Taylor expansion of the potential around these equilibrium positions, the leading term is at second order, which gives the symmetric Hessian matrix

$$H'_{ij} = \frac{1}{\sqrt{m_i m_j}} \frac{\partial^2 U}{\partial z_i \partial z_j}\bigg|_{\{z_i^0\}}. \tag{2}$$

As is typical [48], we use mass-weighted coordinates; we indicate this transformation with a prime, $z'_i = \sqrt{m_i} z_i$. This transformation allows us to write the kinetic energy T in a form that is independent of mass.

The normal modes and their corresponding frequencies can be found by solving the Lagrangian equations of motion for the system. In this case, the relevant quantities are the displacements from equilibrium, $\zeta'_i = z'_i - z_i^{0'}$. Neglecting higher orders in U than those described by (2), the $3N$ equations of motion are

$$\ddot{\zeta}'_j + \sum_{i=1}^{3N} H'_{ij} \zeta'_i = 0. \tag{3}$$

Inserting a fiducial solution $\zeta'_j = \zeta_j^{0'} \mathrm{e}^{\mathrm{i}\omega t}$ gives a linear system of equations that can be diagonalized to yield the normal modes of the system, which are defined by the eigenvalues and eigenvectors of the matrix H'_{ij}. The eigenvalues are equal to ω_α^2, where ω_α is the motional frequency of the normal mode α. The matrix of eigenvectors $\mathrm{e}_i^{\prime\alpha}$ allows us to express normal-mode coordinates as a function of the individual ion coordinates by use of

$$\zeta'_\alpha = \sum_{i=1}^{3N} e_i^{\prime\alpha} \zeta'_i. \tag{4}$$

Since each normal mode acts as an independent oscillator, we can quantize them in the usual manner, writing the mass-weighted position operator as

$$\hat{\zeta}'_\alpha = \sigma'_\alpha \left(\hat{a}_\alpha + \hat{a}_\alpha^\dagger \right), \tag{5}$$

where $\sigma'_\alpha = \sqrt{\hbar/(2\omega_\alpha)}$ and $\hat{a}^\dagger_\alpha$, $\hat{a}_\alpha$ are the raising and lowering ladder operators. For the ith ion in mode α, the ground-state wavefunction root-mean-square size is

$$\sigma_i = \frac{1}{\sqrt{m_i}} e'^{\alpha}_i \sigma'_\alpha. \tag{6}$$

The quantized form for the ion's excursion from equilibrium is [19]

$$\hat{\zeta}_i = \frac{1}{\sqrt{m_i}} \sum_{\alpha=1}^{3N} (e'^{\alpha}_i)^{-1} \sigma'_\alpha \left(\hat{a}_\alpha + \hat{a}^\dagger_\alpha\right). \tag{7}$$

2.1. One-dimensional simplification

For much of the paper, and in many experiments, the trapping potentials are arranged such that ions are confined more strongly in two directions than in the third. The ions then form a linear chain along this third axis, and modes of oscillation involving motion along this axis are of primary interest. For this reason, in section 3 we simplify the treatment by considering a purely axial trap potential centered at $z = 0$, expanded as a power series:

$$V_t(z) = \sum_{n=2}^{\infty} \kappa_n z^n = \kappa_2 z^2 \left[1 + \sum_{n=3}^{\infty} \left(\frac{z}{\lambda_n}\right)^{n-2}\right], \tag{8}$$

where $\lambda_n = (\kappa_n/\kappa_2)^{1/(2-n)}$ is a length used to parameterize the anharmonicity. We will consider potentials where the harmonic ($n = 2$) term dominates, as is typically the case in the experiments described below. In terms of the equation above, we assume $|\Lambda/\lambda_n|^{n-2} \ll 1$, where Λ is some relevant length scale such as the ion chain length L or the ground-state wavepacket size σ. We assume no axial pseudopotential, so the series co-efficients do not depend on the ion mass.

3. Anharmonic modifications to normal modes

For anharmonic perturbations that appear on length scales comparable to that of the ion chain but still negligible on the scale of an ion wave-packet, the main effects are modifications of the normal-mode frequencies and amplitudes. For pairs of ions, these may be examined analytically, and we give examples of cubic and quartic potentials for pairs with equal and with unequal masses. The shifts seen are similar to those in longer chains, which are more easily analyzed numerically. We then examine these effects experimentally. We measure the anharmonic frequency shifts in chains of up to eight ions of equal mass. With mixed-species ion chains, we measure modified mode amplitudes and demonstrate a technique for nulling odd-order anharmonicities.

3.1. Illustrative examples

We start by giving two simple examples with equal-mass ions, which serve to illustrate the main effects that are observed in larger crystals, where numerical methods are more convenient. The parameter $l = (q/8\pi\epsilon_0\kappa_2)^{1/3}$ is a characteristic length scale for the few-ion cases. For example, the distance between two ions in a harmonic well is $L = 2^{1/3} l$. The length of a chain of N ions in a harmonic potential scales as $L \sim l N^{0.37}$, obtained from a fit to numerically calculated chain lengths. In the equal-mass examples below, both cubic and quartic perturbations create a frequency shift that scales as $(l/\lambda_n)^2$. We consider the same perturbations for two unequal mass ions and show that now the frequency shift scales differently in the sizes of the perturbations, $(l/\lambda_n)^{n-2}$. In addition, the cubic perturbation depends on ion-order, while the quartic one does not, allowing the two types of anharmonicity to be differentiated.

3.1.1. Example 1: cubic term with two ions of equal mass. Consider a potential of the form $V_t(z) = (\kappa_2 z^2)(1+z/\lambda_3)$, and assume that $|l/\lambda_3| \ll 1$, i.e. that the cubic term is small compared to the quadratic term over the length scale of the ion separation. The equilibrium positions $z^0_\pm$ are found by solving the set of equations $\partial U/\partial z_i = 0$, which has solutions (to second order in l/λ_3)

$$z^0_\pm \simeq \pm\frac{l}{2^{2/3}}\left[1 \mp \frac{3}{2^{5/3}}\frac{l}{\lambda_3} + \frac{3}{2^{7/3}}\left(\frac{l}{\lambda_3}\right)^2\right]. \tag{9}$$

Expanding the potential about these equilibrium positions, we find that the eigenfrequencies are

$$\omega_{\mathrm{c}} \simeq \sqrt{\frac{2q\kappa_2}{m}}\left[1 - \frac{9}{2^{7/3}}\left(\frac{l}{\lambda_3}\right)^2\right], \tag{10}$$

$$\omega_{\mathrm{s}} \simeq \sqrt{\frac{6q\kappa_2}{m}}\left[1 - \frac{3}{2^{7/3}}\left(\frac{l}{\lambda_3}\right)^2\right]. \tag{11}$$

The corresponding eigenvectors are

$$e'_{\mathrm{c}} \simeq \frac{1}{\sqrt{2}}\begin{pmatrix} 1 - \dfrac{3}{2^{5/3}}\dfrac{l}{\lambda_3} \\ 1 + \dfrac{3}{2^{5/3}}\dfrac{l}{\lambda_3} \end{pmatrix} \tag{12}$$

and

$$e'_{\mathrm{s}} \simeq \frac{1}{\sqrt{2}}\begin{pmatrix} -1 - \dfrac{3}{2^{5/3}}\dfrac{l}{\lambda_3} \\ 1 - \dfrac{3}{2^{5/3}}\dfrac{l}{\lambda_3} \end{pmatrix}. \tag{13}$$

In the limit where $l/\lambda_3 \to 0$ these normal modes would correspond to the center-of-mass and stretch modes. We see from these results that the corrections to the eigenvectors enter at lower order in l/λ_3 than the corrections to the eigenfrequencies, as would be expected from general considerations of perturbation theory [49].

3.1.2. Example 2: quartic term with two ions of equal mass. The quartic term in the trapping potential has been studied for two ions in the context of separation of ions from a single-well potential into a double-well [50], in which the quartic term was as strong as the harmonic term. Here we take an approach similar to that of the previous section and assume it to be small compared to the harmonic term. The potential is then of the form $V_t(z) = \kappa_2 z^2[1+(z/\lambda_4)^2]$, with $|l/\lambda_4|^2 \ll 1$. In this case the center of the ion pair remains at $z = 0$, and the equilibrium positions of the two ions are

$$z_\pm^0 \simeq \pm\frac{l}{2^{2/3}}\left[1 - \frac{1}{3\times 2^{1/3}}\left(\frac{l}{\lambda_4}\right)^2 + \frac{2^{4/3}}{9}\left(\frac{l}{\lambda_4}\right)^4\right]. \tag{14}$$

The normal mode frequencies are

$$\omega_{\rm c} \simeq \sqrt{\frac{2q\kappa_2}{m}}\left[1 + \frac{3}{2^{4/3}}\left(\frac{l}{\lambda_4}\right)^2\right], \tag{15}$$

$$\omega_{\rm s} \simeq \sqrt{\frac{6q\kappa_2}{m}}\left[1 + \frac{5}{3\times 2^{4/3}}\left(\frac{l}{\lambda_4}\right)^2\right]. \tag{16}$$

Note that the frequency shift comes in as $(l/\lambda_n)^2$ for both the quartic and the cubic perturbations. For two ions, the normal-mode amplitudes remain the center-of-mass and stretch modes, as is the case for a purely harmonic potential. For more than two ions, adjacent ions no longer see identical potentials, and the normal-mode amplitudes will shift from their harmonic values.

3.1.3. Example 3: cubic term with two ions of unequal mass. We relax the equal mass assumption of the prior two cases, and re-examine the cubic term for ions with a mass ratio $\mu = m_1/m_2$ (with $z_1 < z_2$). Because of our assumption of no axial pseudopotential, the only mass-dependence is in the kinetic energy, so the ion equilibrium positions are unchanged from (9). The normal-mode frequencies, however, are now

$$\omega_\pm \simeq \sqrt{\frac{2q\kappa_2}{m_1}}\left(1+\mu\pm\sqrt{\mu^2-\mu+1}\right)^{1/2}\left(1 \mp \frac{3}{2^{8/3}}\frac{1-\mu}{\sqrt{\mu^2-\mu+1}}\frac{l}{\lambda_3}\right). \tag{17}$$

Note that the frequency shift is now first-order in l/λ_3 and depends on the ion order due to the first-order dependence on the sign of l/λ_3. In the limit of a purely harmonic potential, (17) reproduces the results of [19, 51]. The normal-mode eigenvectors are

$$e'_\pm \simeq \frac{1}{\sqrt{1+r_\pm^2}}\begin{pmatrix} r_\pm\left[\mp 1 - \frac{3}{2^{5/3}}\frac{1+\mu}{\sqrt{\mu^2-\mu+1}}\frac{1}{1+r_\pm^2}\frac{l}{\lambda_3}\right] \\ 1 \mp \frac{3}{2^{5/3}}\frac{1+\mu}{\sqrt{\mu^2-\mu+1}}\frac{r_\pm^2}{1+r_\pm^2}\frac{l}{\lambda_3}\end{pmatrix}. \tag{18}$$

Here, $r_\pm = [\pm(\mu-1)+\sqrt{\mu^2-\mu+1}]/\sqrt{\mu}$. As for the equal-mass case, the higher-frequency mode (subscript +) involves the ions moving out of phase and the other mode involves in-phase motion. As before, the mode-amplitude corrections scale as l/λ_3, though with mass-dependent coefficients.

3.1.4. Example 4: quartic term with two ions of unequal mass. For unequal-mass ions in a potential with a quartic perturbation, the normal-mode frequencies are

$$\omega_\pm \simeq \sqrt{\frac{2q\kappa_2}{m_1}}\left(1+\mu\pm\sqrt{\mu^2-\mu+1}\right)^{1/2}\left[1 + \frac{1}{3\times 2^{4/3}}\frac{\mp(1+\mu)+7\sqrt{\mu^2-\mu+1}}{\sqrt{\mu^2-\mu+1}}\left(\frac{l}{\lambda_4}\right)^2\right]. \tag{19}$$

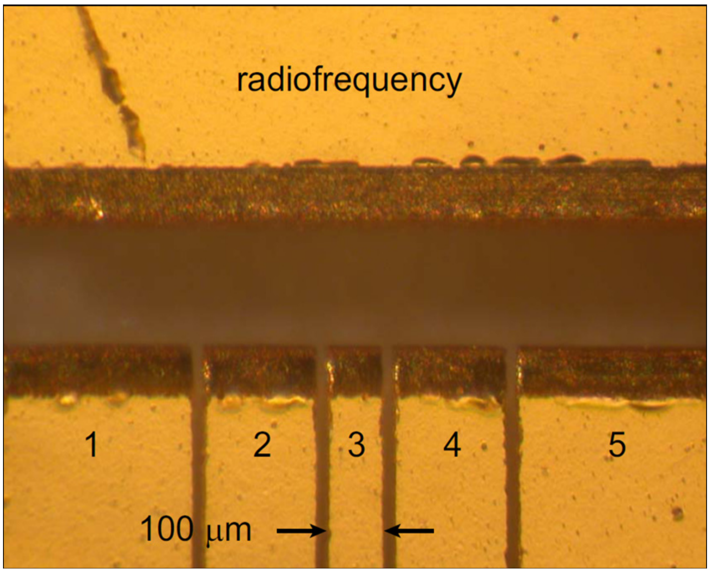

Figure 1. A top view of one of the gold-plated alumina wafers that combines with a second underlying wafer to trap the ions. The picture encompasses the electrodes in the region used in the experiments.

In this case, the frequency shift is second-order in l/λ_4, as for the equal mass ions. As one would expect from the symmetry of the potential, the frequencies do not depend on ion order. The eigenvectors are

$$e'_{\pm} \simeq \frac{1}{\sqrt{1+r_{\pm}^2}} \begin{pmatrix} r_{\pm}\left[\mp 1 - \dfrac{1}{2^{1/3}} \dfrac{1-\mu}{\sqrt{\mu^2-\mu+1}} \dfrac{1}{1+r_{\pm}^2} \left(\dfrac{l}{\lambda_4}\right)^2\right] \\ 1 \pm \dfrac{1}{2^{1/3}} \dfrac{1-\mu}{\sqrt{\mu^2-\mu+1}} \dfrac{r_{\pm}^2}{1+r_{\pm}^2} \left(\dfrac{l}{\lambda_4}\right)^2 \end{pmatrix}. \qquad (20)$$

Unlike the equal-mass case, the different masses break the symmetry, and there are quartic corrections to the mode amplitudes.

3.2. *Experimental demonstrations*

Using various combinations of $^9\mathrm{Be}^+$ and $^{24}\mathrm{Mg}^+$, we demonstrate normal-mode frequency and amplitude shifts arising from weak anharmonic perturbations. We also present a technique that uses the ion order of an unequal-mass pair to suppress odd-order anharmonicities.

3.2.1. Ion trap and potential wells. The linear radiofrequency Paul trap used here (described in [25]) stores the $^9\mathrm{Be}^+$ and $^{24}\mathrm{Mg}^+$ ions. The trap is formed from two 125 μm thick wafers of alumina, with the electrodes made of sputtered gold and laser-cut 20 μm vacuum gaps between adjacent electrodes. A top view of the top wafer in the relevant region of the trap is shown in figure 1. Radial confinement of the ions is provided by a pseudopotential derived from a quadrupole potential ($V_{\mathrm{peak}} \sim 200$–$300$ V) oscillating at a radio frequency ($\Omega_{\mathrm{rf}} = 2\pi \times 150$ MHz) and resulting in radial secular frequencies of approximately 12 MHz for a single $^9\mathrm{Be}^+$

ion. The experimental region of the trap has five pairs of control electrodes that can be used to create axial potential wells (the trap has three additional pairs of control electrodes, but these are placed far from the experimental region and have only a small effect on the axial potentials in this region). The pairs of electrodes are arranged such that one of each pair is on the top wafer and the other opposes it on the bottom wafer [24]. The nominal voltage applied to the electrodes in one pair is the same; however a (typically small) differential component is also used to null out stray static electric fields at the pseudopotential zero as well as the effects of trap imperfections. In order to design potential wells for the ions located at a particular position, we simulate the influence of each electrode at that position using the boundary element method (BEM) [52]. Since the fields from each electrode can be superposed, this allows us to design sets of voltages that produce harmonic or anharmonic potential wells at any point along the trap axis. It should be noted that while the simulation provides guidance, it relies on dimensions taken from photos of the actual trap, and thus its accuracy is limited.

For the quantum information experiments performed in this trap [14, 25, 26], we used two base sets of potentials. We periodically adjusted them with shim voltages or scaled them to adjust motional frequencies, but most experiments and waveforms began and ended with one of these sets. The first set produced a single potential well, positioned close to electrode 2, with negligible anharmonic terms along the axis of the trap. Despite our assumption above, slight electrode asymmetries can produce a small axial pseudopotential; therefore we designed this potential well to overlap its minimum position with the axial pseudopotential minimum, which we found experimentally. The voltage configuration used to do this was $\boldsymbol{V}^{(1)} = \{3.7, 1.3, 1.5, 4.1, 3.7\}$ V, where the numbers indicate the voltage applied to electrode pairs 1 to 5. The simulated potential produced by these voltages is shown in figure 2(a). The quantum information experiments required simultaneous trapping of ions in two experiment zones, for which we used the double-well potential shown in figure 2(b). This potential used the voltage set $\boldsymbol{V}^{(2)} = \{3.8, 0.0, 2.8, 0.0, 3.7\}$ V, producing two potential wells 240 μm apart. Both the single-well and the double-well potentials were designed to produce a minimum at the same position, $-120\,\mu$m in figure 2, with the same curvature, $\kappa_2 = m\omega_z^2/(2q) = 1.3 \times 10^7$ V m^{-2}, corresponding to $\omega_z = 2\pi$ (2.7 MHz) and $l = 3.8\,\mu$m for beryllium ions. From BEM simulations of the potential, we estimate the anharmonic terms of the double-well potential to be $\lambda_3 = -200\,\mu$m and $\lambda_4 = 250\,\mu$m. By comparison, simulations of the single-well potential give $\lambda_3 = 10$ mm and $\lambda_4 = 1$ mm.

3.2.2. Control and readout of trapped ions. Control of the ions' internal states and motion is primarily through standard techniques described elsewhere [25, 35]. A 11.964 mT magnetic field establishes a quantization axis aligned at 45° to both the trap axis and the vector normal to the alumina wafers. The ions' motion is initially Doppler laser cooled to temperatures low enough that the root-mean-square motional wavefunction size of each mode is less than 100 nm. For some experiments, we proceed with cooling one or more modes to near the ground state by use of Raman sideband transitions. The ^{9}Be$^+$ ions' internal states are initialized by optical pumping to the $\mathrm{S}_{1/2}|F = 2, M_F = 2\rangle$ hyperfine level, which we label as $|i\rangle$. To observe and Doppler cool the ions, we use a 313 nm σ^+-polarized laser beam tuned close to resonance with the $|i\rangle \leftrightarrow \mathrm{P}_{3/2}\ |F' = 3, M_F' = 3\rangle$ closed cycling transition. State-dependent resonant fluorescence from the ions is detected on a photomultiplier tube (PMT) during a 200 μs detection window. For an ion initialized in $|i\rangle$, we observe an average of approximately eight counts on the PMT.

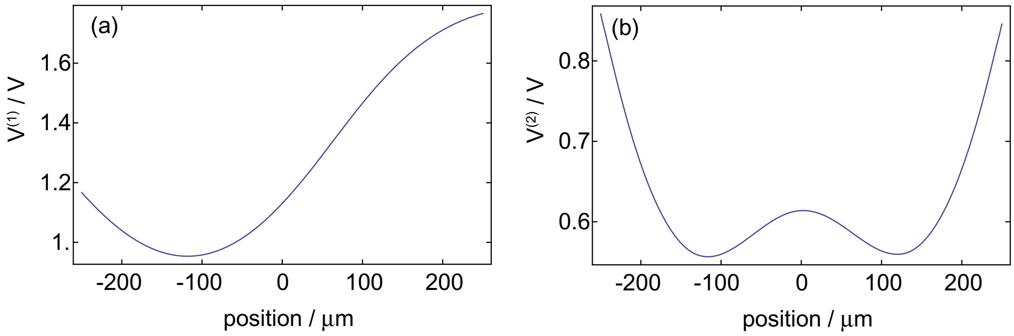

Figure 2. Simulations of the two axial trapping potentials. The origin of the position co-ordinate is in the center of electrode 3. (a) The harmonic-potential well, designed to have negligible anharmonic terms along the axis of the trap. (b) The double-well potential, which has significant anharmonicities in both wells.

Transitions among internal and motional states of the $^9\mathrm{Be}^+$ ions are induced by stimulated Raman interactions. These use two laser beams derived from the same laser; the pair of beams has a relative detuning equal to that of a hyperfine 'carrier' transition or a hyperfine transition plus or minus a motional frequency ('sideband' transitions). The laser is detuned $-70\,\mathrm{GHz}$ from the $S_{1/2} \leftrightarrow P_{1/2}$ transition. The geometry of the beams relative to the ions determines whether the lasers interact with only the internal states or with the motion as well. For motion-sensitive transitions, both beams are aligned at 45° to the axis of the trap (one anti-parallel and one perpendicular to the magnetic field), with their difference vector $\boldsymbol{\delta k}$ aligned along the axis, with a magnitude of $|\delta k| = 2\pi \times \sqrt{2}/\lambda$, where $\lambda = 313\,\mathrm{nm}$. We typically utilize transitions between the states $|\downarrow\rangle \equiv \mathrm{S}_{1/2}|F=2, M_F=1\rangle$ and $|\uparrow\rangle \equiv \mathrm{S}_{1/2}|F=1, M_F=0\rangle$, whose frequency difference has no first-order sensitivity to magnetic field [46]. In order to make use of this transition, we first transfer population from $|i\rangle \rightarrow |\downarrow\rangle$, again with a stimulated Raman interaction. Subsequent to driving Raman transitions on $|\downarrow\rangle \leftrightarrow |\uparrow\rangle$, we transfer $|\downarrow\rangle \rightarrow |i\rangle$ and $|\uparrow\rangle \rightarrow \mathrm{S}_{1/2}|F=1, M_F=-1\rangle$, where the latter has no transitions that are close to resonance with the detection laser frequency and thus gives negligible fluorescence.

To measure trap frequencies, we resonantly excite the motion of the ions. An oscillating 'tickle' voltage is applied to one electrode of the trap, resulting in an oscillating electric field at the position of the ions. This excites motion when tuned close to resonance with a normal mode. Large motional excitations ($\bar{n} > 100$) may be observed as a decrease in fluorescence of state $|i\rangle$, but motion-sensitive stimulated Raman transitions enable the detection of motional excitation corresponding to a single quantum. Each method will be described in detail below.

3.3. Frequency shifts, homogeneous ion crystals

One way to characterize the anharmonicities is to examine the axial frequencies of the in-phase motion of chains of $^9\mathrm{Be}^+$ ions as a function of the number of ions in the chain. With the ions initialized in the internal state $|i\rangle$, we apply the tickle voltage for 500 μs and subsequently detect. A resonant force significantly excites the motion, resulting in a drop in the ion fluorescence level (see for example [53]) as the ions' Doppler shifts approach the linewidth of the optical

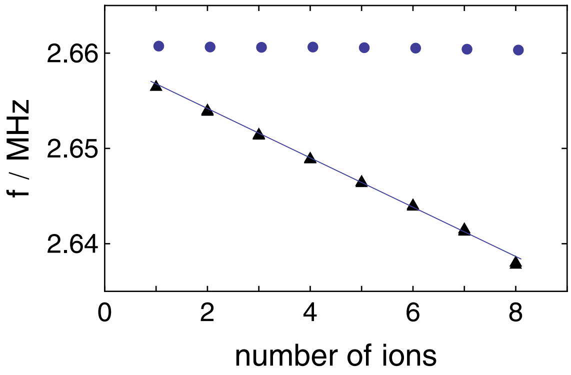

Figure 3. The frequency of the center-of-mass mode as a function of the number of ^{9}Be^{+} ions. Triangles indicate the frequencies measured in the anharmonic trap given by potentials $\boldsymbol{V}^{(2)}$; circles indicate the frequencies in the harmonic trap given by potentials $\boldsymbol{V}^{(1)}$. The line is a fit to the anharmonic trap's frequency shift. Error bars are smaller than the symbols.

transition (for the fluorescence to drop to one half requires an excitation of approximately 1000 phonons for typical trap frequencies). For each frequency setting of the tickle voltage, we repeat the experiment 500 times, and record the average number of photon counts observed during the 200 μs detection period. We fit the results with a Lorentzian to obtain the normal-mode frequency.

The resonant frequencies for the in-phase mode of motion of linear chains of one to eight ^{9}Be^{+} ions in the potentials created by $\boldsymbol{V}^{(1)}$ and $\boldsymbol{V}^{(2)}$ are shown in figure 3. For the nearly harmonic well, the in-phase mode frequency changes by $-0.4(1)$ kHz between one ion and eight ions, an effect that is negligible on the plotted scale. However in the case of the more anharmonic potential well, there is a frequency shift of $-2.59(3)$ kHz per ion. Both the cubic and quartic terms produce a linear frequency shift per ion up to eight ions, so we are unable to distinguish these components in this type of experiment.

3.4. Frequency shifts, inhomogeneous ion crystals

To isolate only the odd-order components of the anharmonicity, we make use of an asymmetric ion chain, here consisting of one ^{9}Be^{+} and one ^{24}Mg^{+} ion. We deterministically order the ions as ^{9}Be^{+}– ^{24}Mg^{+} or ^{24}Mg^{+}– ^{9}Be^{+} (see below). The length of the pair is $L = 4.8\,\mu$m. Odd-order anharmonicities produce different frequency shifts for different ion order, whereas even terms produce identical shifts.

The mass difference between the ions and the mass dependence of the radial pseudopotential allow deterministic initialization of the ion order [54–56]. The re-ordering proceeds by first applying a radial electric field under continuous Doppler cooling so the ions remain close to their equilibrium positions. This field displaces the ^{24}Mg^{+} ion more than the ^{9}Be^{+} one due to the weaker pseudopotential experienced by the heavier-mass ion. At a critical value of the electric field the axis of the two-ion crystal is normal to the trap axis. At this point, a differential shim voltage between upper and lower electrodes (e.g. electrodes 2-upper and 4-lower raised relative to 2-lower and 4-upper) can twist the axis of the static potential, breaking its symmetry relative to the orientation of the two ions, and pushing the ^{24}Mg^{+} to one side of

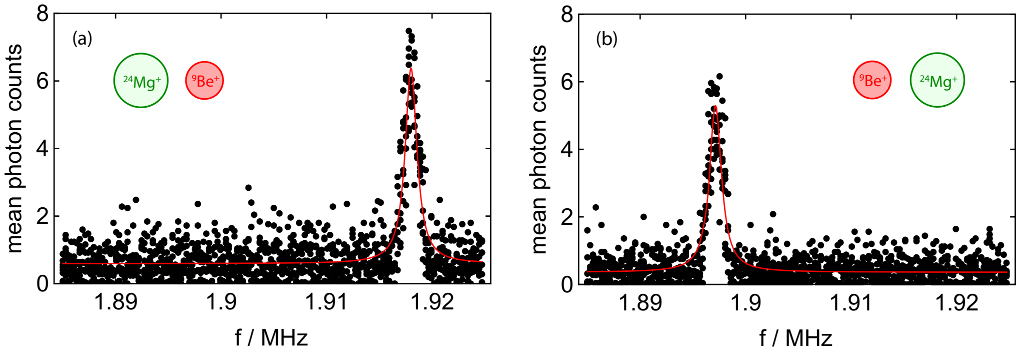

Figure 4. Frequency of the in-phase mode for ions in the order (a) ^{24}Mg^{+}– ^{9}Be^{+} and (b) ^{9}Be^{+}– ^{24}Mg^{+} in the anharmonic well situated at $-120\,\mu$m in figure 2.

the ^{9}Be^{+} ion along the trap axis. By subsequently reducing the field and removing the twist, the ions are left in the desired order.

After ordering the ions, the frequency of the in-phase normal mode of the two ions is measured by use of the tickle method. In the case of two ions of unequal mass, both axial modes of motion involve modulation in the distance between the ions. This means that anharmonicity in the Coulomb interaction can produce frequency shifts on both modes as a function of motional excitation [20]. These shift the deduced motional frequency, and can prevent a single frequency drive from exciting the ions to energies high enough to reduce fluorescence.

To reduce the excitation energy at which a signal can be observed, we can observe weak motional excitation using Raman transitions. We first initialize both axial modes of the ion chain close to the ground state of motion by use of Raman sideband cooling [57]. After applying the tickle, we probe the motional excitation of the ^{9}Be^{+} ion by resonantly driving the $|{\downarrow}\rangle \leftrightarrow |{\uparrow}\rangle$ carrier transition with the motion-sensitive Raman beams. We choose the drive duration such that an ion in the ground state would make a full transition from from $|{\downarrow}\rangle \rightarrow |{\uparrow}\rangle$, which would leave a subsequent detection 'dark'. If the motion of a normal mode is excited to state $|n\rangle$, the transition rate is reduced by a factor given by the matrix element $\langle n|\exp(\mathrm{i}\eta(\hat{a}+\hat{a}^{\dagger}))|n\rangle$, where $\eta = \delta k\,\sigma$ is the Lamb–Dicke parameter [35]. This results in incomplete population transfer, resulting in the detection of fluorescence in the subsequent detection window. For the in-phase mode of motion of a ^{9}Be^{+}– ^{24}Mg^{+} pair, $\eta = 0.18$, and the Rabi frequency of the transition is reduced to approximately half the ground-state rate for $n = 17$. A more precise description involves averaging the transferred population over the Fock state distribution of a coherent state, however the current estimate is sufficient for our present purposes.

Data from frequency scans of the tickle voltage applied near the in-phase axial mode frequency for two configurations of ions in the anharmonic potential well characterized by $\boldsymbol{V}^{(2)}$ are shown in figure 4. The data sets are each fitted with a Lorentzian, and the frequency of the normal mode extracted. We measure a difference of 20.8(2) kHz between the mode frequencies for the two configurations. If the only odd-order component is a cubic term, this corresponds to $\lambda_3 = -230\,\mu$m. By comparison, a similar experiment performed in the more harmonic well characterized by $\boldsymbol{V}^{(1)}$ gives a frequency shift of less than 0.03(2) kHz, corresponding to $|\lambda_3| > 150$ mm.

An even more sensitive method of observing motional excitation is to probe on a motional sideband of the $|{\downarrow}\rangle \leftrightarrow |{\uparrow}\rangle$ transition. If the motional mode is in the ground state the motion-subtracting sideband cannot be driven. However, when the motion is excited, population transfer is allowed between $|\downarrow\rangle$ and $|\uparrow\rangle$. To maximize the population in $n = 1$ (for which the Rabi frequency is set to make a full transfer), we would require the tickle to excite the motion to a coherent state [58] with $\alpha \approx 1$. A coherent state of this size would result in half the population being transferred from $|\downarrow\rangle$ to $|\uparrow\rangle$. We use this method for nulling anharmonicity as described in section 3.5.

3.4.1. Measurement of modified ion amplitudes. When driving motion-sensitive Raman transitions, the amplitude of motion of the ion in the normal mode affects the modulation index of the light, thus affecting the Rabi frequency at which the mode is driven. Mathematically, for ion j, the transition matrix element for the resonant transition between $|\downarrow_j, n\rangle$ and $|\uparrow_j, n+1\rangle$ is proportional to $\langle n|\exp[\mathrm{i}\delta k\,\sigma_j(\hat{a}+\hat{a}^\dagger)]|n+1\rangle$ [35], where σ_j is given in (6) and is proportional to the ion's motional amplitude through the mode's eigenvector. For $\sigma_j \ll 1/\delta k$, this expression reduces to $\delta k\,\sigma_j\sqrt{n+1}$, showing direct proportionality to the amplitude.

In the experiment, we use a four-ion chain containing two $^{9}\mathrm{Be}^{+}$ and two $^{24}\mathrm{Mg}^{+}$ ions, which are initialized in the order $^{9}\mathrm{Be}^{+}$– $^{24}\mathrm{Mg}^{+}$– $^{24}\mathrm{Mg}^{+}$– $^{9}\mathrm{Be}^{+}$ prior to each run of the experimental sequence [25]. Only the beryllium ions interact with the 313 nm Raman light fields. The length of the chain is $L = 10.8\,\mu\mathrm{m}$.

To equalize the intensity of each Raman light field on the two $^{9}\mathrm{Be}^{+}$ ions, we separately observe the ac Stark shift of each beam. Either beam alone cannot drive a transition between $|\downarrow\rangle$ and $|\uparrow\rangle$, but the light causes a phase shift that we monitor with a Ramsey-type interference experiment [59] where one beam is applied between the two Ramsey pulses. By equalizing the rates at which these phases evolve for both ions, we equalize the relative electric field strength of each light field at each ion to better than 2%.

Once the light fields are equalized on the ions, we drive motional sidebands of the four-ion chain. The two highest-frequency axial modes have frequencies of $f_3 = 5.5\,\mathrm{MHz}$ and $f_4 = 5.7\,\mathrm{MHz}$ and are particularly sensitive to the cubic term in the axial potential. In the nearly harmonic potential they have normal-mode eigenvectors $\boldsymbol{e}'_3 = (0.629, -0.322, -0.322, 0.629)$ and $\boldsymbol{e}'_4 = (0.532, -0.465, 0.465, -0.532)$. In the more anharmonic potential, the amplitudes are significantly different. This becomes obvious when the internal state populations are measured as a function of sideband drive duration, where beating behavior is observed due to the different Rabi rates of each ion. Results of such measurements are shown in figure 5. Also shown are simulations of sideband drives for two $^{9}\mathrm{Be}^{+}$ ions with a ratio of amplitudes of ion motion ($R_\alpha = |e'_{\alpha 1}/e'_{\alpha 4}|$) of $R_3 = 0.625$ and $R_4 = 0.500$ (these values were chosen by eye to best fit the data). The simulation curves are obtained by integrating the Schrödinger equation, and subsequently adding a phenomenological decay to the Rabi oscillations in order to account for both motional and internal-state decoherence. Both simulations use the same value of the carrier Rabi frequency. For the cubic term of $\lambda_3 = -230\,\mu\mathrm{m}$ obtained from the frequency shifts of the $^{9}\mathrm{Be}^{+}$– $^{24}\mathrm{Mg}^{+}$ in-phase mode, we would expect these ratios to be $R_3 = 0.644$ and $R_4 = 0.499$. The eigenvectors in this case are $\boldsymbol{e}'_3 = (0.474, -0.167, -0.452, 0.736)$ and $\boldsymbol{e}'_4 = (0.686, -0.531, 0.359, -0.342)$. Though the agreement between the two values of R_3 seems good, choosing $R_3 = 0.644$ produces a noticeable mismatch between data and theory. The reason for this discrepancy is currently not understood.

Unequal amplitudes of motion are generally undesirable for performing multi-qubit logic gates on trapped ions. For the gate methods in common use today [11, 13, 60, 61], driven ion motion during the gate adds a phase conditioned on the qubits' joint state. In these gates, the

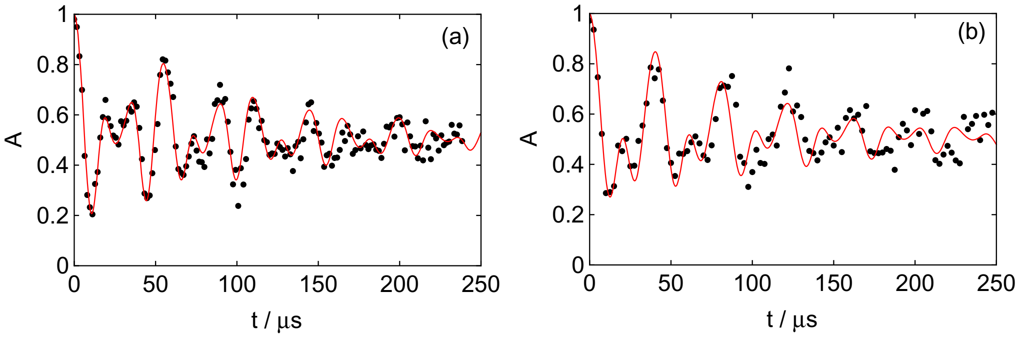

Figure 5. Experimental results and numerical simulations of sideband flopping on the two beryllium ions for (a) the third and (b) the fourth axial mode of a four-ion $^{9}Be^{+}$– $^{24}Mg^{+}$– $^{24}Mg^{+}$– $^{9}Be^{+}$ chain in the anharmonic trap. The amplitude is related to the population of ions in the $|\uparrow\rangle$ state, $A = P(\uparrow\uparrow) + [P(\uparrow\downarrow) + P(\downarrow\uparrow)]/2$, and is proportional to the total fluorescence from both ions.

unequal mode amplitudes can lead to a longer required gate duration, thereby increasing the probability of error from off-resonant photon scattering [62]. Additionally, this phase could be different for $|\uparrow\downarrow\rangle$ and $|\downarrow\uparrow\rangle$ due to the different ion-amplitudes, which increases the complexity of gate calibration.

3.5. *Nulling odd-order anharmonicities*

For the purposes of optimizing quantum logic gates on multi-ion crystals, it is desirable to be able to tune out the anharmonicities. In the trap used here, we cannot do this while maintaining a double-well potential if the positions of the minima of the two potential wells are fixed to be the same as the minima of the set of potentials $\boldsymbol{V}^{(2)}$ (the number of independent electrode voltages is insufficient to satisfy all the required constraints). However, if we remove this position constraint, it is possible to produce two wells with zero odd-order anharmonicity (though it seems that one voltage should not be sufficient to meet the constraints of the two wells, in practice the symmetry of the electrodes with respect to the well positions is sufficient to meet both constraints). We perform this optimization by observing the ion-order dependence of the in-phase and out-of-phase mode frequencies of a $^{9}Be^{+}$– $^{24}Mg^{+}$ pair as a function of the voltage V_3 applied to the control electrode positioned between the two potential wells. The potentials used here are slightly modified from $\boldsymbol{V}^{(2)}$ and are optimized in simulation for negligible cubic anharmonicity in both wells. The nulling procedure allows *in situ* adjustment to account for differences between simulation and experiment.

Data from such an optimization are shown in figure 6, which shows frequency differences when reversing ion order for the potential well close to electrode 2 in the double-well potential. The data show that the value of V_3 where the in-phase mode shows zero frequency shift on inverting the ion order is different from the value of V_3, where the same condition is met for the out-of-phase mode. This discrepancy is consistent with a small pseudopotential gradient along the axis of the trap, indicating that the adjusted position is no longer at the axial pseudopotential minimum. Since the pseudopotential has a different strength for both ions, a gradient pointing from $^{24}Mg^{+}$ to $^{9}Be^{+}$ will result in the spacing of the ions being reduced (and vice versa). This tends to increase the energy of the out-of-phase mode, but has a smaller impact on the in-phase

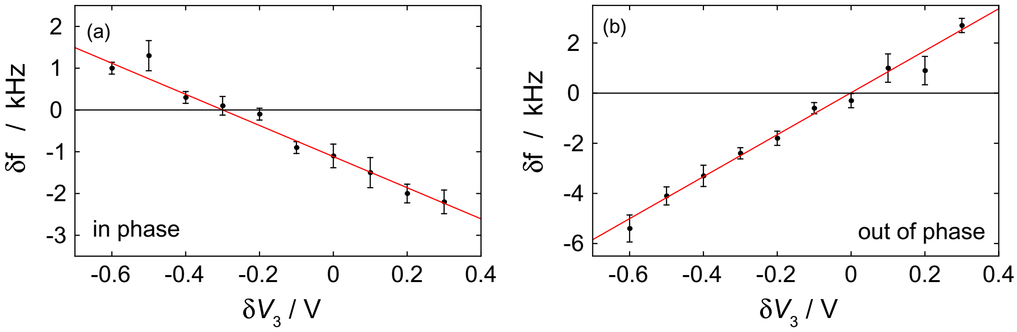

Figure 6. Ion-order-dependent frequency shift for the potential well close to electrode 2 in the double-well potential. The (a) in-phase and (b) out-of-phase mode frequency between the $^{24}\mathrm{Mg}^{+}$– $^{9}\mathrm{Be}^{+}$ and $^{9}\mathrm{Be}^{+}$– $^{24}\mathrm{Mg}^{+}$ configurations as a function of electrode 3 voltage, which is plotted as an offset from the simulated value.

mode. From the shift of the out-of-phase mode at the point where the in-phase shift is nulled, we can calculate a value of the pseudopotential gradient of $0.2\,\mathrm{eV\,m^{-1}}$.

To choose which value of V_3 to use to minimize the $^{9}\mathrm{Be}^{+}$– $^{24}\mathrm{Mg}^{+}$– $^{24}\mathrm{Mg}^{+}$– $^{9}\mathrm{Be}^{+}$ sideband amplitude imbalance described in the previous section, we numerically calculated the amplitude imbalance with the pseudopotential gradient fixed. We find that the parameters for which the amplitudes are balanced are close to those for which the $^{9}\mathrm{Be}^{+}$– $^{24}\mathrm{Mg}^{+}$ in-phase mode shift is minimized. For this condition, the resulting amplitudes for the four ion chain are calculated to be $\boldsymbol{e}_3' = (0.631, -0.323, -0.322, 0.628)$ and $\boldsymbol{e}_4' = (0.530, -0.465, 0.467, -0.533)$.

4. Strong anharmonic effects: modifications to the normal-mode picture

As anharmonic effects increase to the level where individual ions sample the anharmonicity during excursions about equilibrium (that is, σ/λ_n is no longer negligible), the independent normal-mode picture for ion motion is no longer valid. The anharmonicities lead to coupling between the normal modes. The principal effects of this coupling are mode frequency shifts as a function of the number of quanta in both the motional mode of interest and other motional modes. Anharmonic effects of this kind were observed in [20], where the mode cross-coupling was due to anharmonicity in the Coulomb interaction between two ions. A variety of couplings due to the Coulomb anharmonicity are also discussed in [63]. In what follows, we extend these results by considering shifts arising from an arbitrary applied trapping potential. As a concrete example, we evaluate this in the context of a surface-electrode trap with the ion trapped $30\,\mu\mathrm{m}$ above the electrode plane.

4.1. Perturbation theory

If the harmonic term still dominates the potential energy, we may treat anharmonicity as a perturbation. Our goal is to calculate the frequency shift Δf_Z of a given mode (labeled Z in this section) for the transition between n_Z and $n_Z + 1$. The shift may depend on the occupation of that mode n_Z, as well as that of all other modes $\{n_\alpha\}$. Because of the potential dependence on other modes, we again consider all three dimensions, as we did in section 2, and revert to the notation used in that section. The cubic and quartic terms in a Taylor expansion of the potential energy U will involve sums over the coefficients

$$A'^{(3)}_{ijk} = \frac{1}{3!}\frac{1}{\sqrt{m_i m_j m_k}}\frac{\partial^3 U}{\partial z_i \partial z_j \partial z_k}\bigg|_{\{z_i^0\}}, \tag{21}$$

$$A'^{(4)}_{ijkl} = \frac{1}{4!}\frac{1}{\sqrt{m_i m_j m_k m_l}}\frac{\partial^4 U}{\partial z_i \partial z_j \partial z_k \partial z_l}\bigg|_{\{z_i^0\}}, \tag{22}$$

where the indices refer to ions not normal modes. Both the Coulomb interaction and any anharmonic terms in the trapping potential contribute to these coefficients.

Because we are interested in perturbations to the normal modes of the system, we transform these tensors into the normal-mode basis in a manner analogous to the vector case of (3):

$$G'^{(3)}_{\alpha\beta\gamma} = \sigma'_\alpha \sigma'_\beta \sigma'_\gamma \sum_{i,j,k} e'^{i}_{\alpha}\, e'^{j}_{\beta}\, e'^{k}_{\gamma}\, A'^{(3)}_{ijk}, \tag{23}$$

$$G'^{(4)}_{\alpha\beta\gamma\delta} = \sigma'_\alpha \sigma'_\beta \sigma'_\gamma \sigma'_\delta \sum_{i,j,k,l} e'^{i}_{\alpha}\, e'^{j}_{\beta}\, e'^{k}_{\gamma}\, e'^{l}_{\delta}\, A'^{(4)}_{ijkl}. \tag{24}$$

The inclusion of the σ' coefficients is for notational convenience. In this notation, the cubic and quartic terms of the Taylor expansion are

$$U^{(3)} = \sum_{\alpha,\beta,\gamma} G'^{(3)}_{\alpha\beta\gamma}(\hat{a}_\alpha + \hat{a}^\dagger_\alpha)(\hat{a}_\beta + \hat{a}^\dagger_\beta)(\hat{a}_\gamma + \hat{a}^\dagger_\gamma), \tag{25}$$

$$U^{(4)} = \sum_{\alpha,\beta,\gamma,\delta} G'^{(4)}_{\alpha\beta\gamma\delta}(\hat{a}_\alpha + \hat{a}^\dagger_\alpha)(\hat{a}_\beta + \hat{a}^\dagger_\beta)(\hat{a}_\gamma + \hat{a}^\dagger_\gamma)(\hat{a}_\delta + \hat{a}^\dagger_\delta). \tag{26}$$

Here, we have written the position operator $\hat{\zeta}'_\alpha$ in terms of raising and lowering operators as in (5).

In first-order perturbation theory, all odd-order contributions vanish exactly and the leading contribution is from the quartic term:

$$\Delta E_1(n_\alpha, n_\beta, n_\gamma, n_\delta) = \left\langle n_\alpha, n_\beta, n_\gamma, n_\delta \left| U^{(4)} \right| n_\alpha, n_\beta, n_\gamma, n_\delta \right\rangle. \tag{27}$$

Only terms with coefficients $G'^{(4)}_{ZZZZ}$ and $G'^{(4)}_{\alpha\alpha ZZ}$ have nonzero contributions to the $n_Z \leftrightarrow n_Z + 1$ frequency shift.

The cubic terms give the leading contribution in second-order perturbation theory,

$$\Delta E_2\left(n_\alpha, n_\beta, n_\gamma\right) = \sum_{\substack{\{\tilde{n}_\alpha, \tilde{n}_\beta, \tilde{n}_\gamma\} \\ \neq \{n_\alpha, n_\beta, n_\gamma\}}} \frac{\left|\left\langle \tilde{n}_\alpha, \tilde{n}_\beta, \tilde{n}_\gamma \left| U^{(3)} \right| n_\alpha, n_\beta, n_\gamma \right\rangle\right|^2}{\hbar\left[\omega_\alpha\left(n_\alpha - \tilde{n}_\alpha\right) + \omega_\beta\left(n_\beta - \tilde{n}_\beta\right) + \omega_\gamma\left(n_\gamma - \tilde{n}_\gamma\right)\right]}. \tag{28}$$

These terms can potentially lead to a number of resonances. For example, it is possible for two modes to have a resonance allowing the destruction of two phonons from one of the modes and the creation of one phonon in the other. The $G'^{(3)}_{\alpha\alpha Z}$ term in the potential creates such an interaction. In this discussion, we assume we are detuned from all such resonances so that perturbation theory remains valid. As ion numbers increase, mode density will increase and it will be harder to avoid these resonances.

After evaluating the ladder-operator algebra for the leading perturbation-theory contributions above, we find that the frequency shift for the $n_Z \leftrightarrow n_Z+1$ transition is

$$
\begin{aligned}
h\Delta f_Z(\{n_\alpha\}, n_Z) = {} & \Delta E_1(\{n_\alpha\}, n_Z+1) - \Delta E_1(\{n_\alpha\}, n_Z) \\
& + \Delta E_2(\{n_\alpha\}, n_Z+1) - \Delta E_2(\{n_\alpha\}, n_Z) \\
= {} & 12\left[(n_Z+1)\,G'^{(4)}_{ZZZZ} + \sum_{\alpha\neq Z}^{3N} G'^{(4)}_{\alpha\alpha ZZ}\,(1+2n_\alpha)\right] \\
& - \frac{36}{\hbar}\sum_{\alpha\neq Z}^{3N}(2n_\alpha+1)\left[\frac{2\omega_\alpha (G'^{(3)}_{\alpha\alpha Z})^2}{4\omega_\alpha^2-\omega_Z^2} + \frac{2\omega_Z (G'^{(3)}_{ZZ\alpha})^2}{4\omega_Z^2-\omega_\alpha^2}\right. \\
& \left. + \frac{G'^{(3)}_{ZZZ}G'^{(3)}_{\alpha\alpha Z}}{\omega_Z} + \frac{G'^{(3)}_{\alpha ZZ}G'^{(3)}_{\alpha\alpha\alpha}}{\omega_\alpha}\right] - \frac{6}{\hbar}(n_Z+1) \\
& \times \left[10\frac{(G'^{(3)}_{ZZZ})^2}{\omega_Z} - 6\sum_{\alpha\neq Z}^{3N}\frac{(G'^{(3)}_{ZZ\alpha})^2\omega_\alpha}{4\omega_Z^2-\omega_\alpha^2} + 12\sum_{\alpha\neq Z}^{3N}\frac{(G'^{(3)}_{\alpha ZZ})^2}{\omega_\alpha}\right] \\
& - \frac{72}{\hbar}\sum_{\alpha\neq Z}^{3N}\sum_{\beta\neq Z,\alpha}^{3N}(G'^{(3)}_{\alpha\beta Z})^2\left[\frac{(n_\alpha-n_\beta)(\omega_\beta-\omega_\alpha)}{(\omega_\beta-\omega_\alpha)^2-\omega_Z^2} + \frac{(n_\alpha+n_\beta+1)(\omega_\beta+\omega_\alpha)}{(\omega_\beta+\omega_\alpha)^2-\omega_Z^2}\right] \\
& - \frac{36}{\hbar}\sum_{\alpha\neq Z}^{3N}\frac{G'^{(3)}_{\alpha ZZ}}{\omega_\alpha}\left[\sum_{\beta\neq Z,\alpha}^{3N} G'^{(3)}_{\alpha\beta\beta}(2n_\beta+1)\right].
\end{aligned}
\tag{29}
$$

4.2. Example case: a microfabricated surface trap

One of the smaller traps that has been used at NIST has the electrodes lying in a plane and $^{25}\mathrm{Mg}^+$ ions trapped 30 μm above that surface (a nearly identical trap was used in [64]). Figure 7 shows the trap geometry. The trap is operated with single-ion secular frequencies for the radial modes of $f_1 = 7$ MHz and $f_2 = 5$ MHz, and an axial frequency of $f_3 = 1.8$ MHz. The asymmetry of the trap electrodes with respect to the position of the ion creates cubic perturbations in directions out of the plane of the trap that dominate the third-order tensor $G'^{(3)}$.

Using (29), we calculate a cross-coupling matrix χ, which relates mode frequency shifts to excitation through

$$\Delta f_Z = \sum_{\alpha=1}^{3N} \chi_{Z\alpha}\, n_\alpha. \tag{30}$$

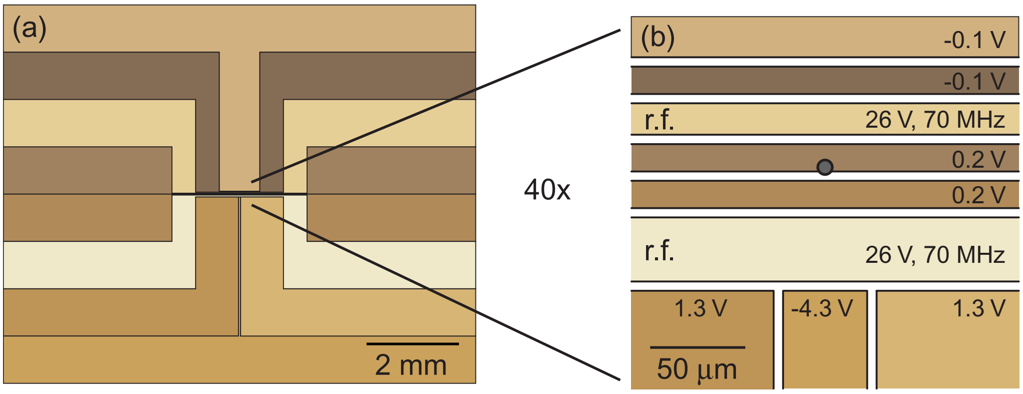

Figure 7. Diagram of (a) a microfabricated surface-electrode trap and (b) a closer view at the trapping region. Colors differentiate the electrodes, which are marked with their bias voltages. The radiofrequency electrodes are at dc ground. A single ion would be trapped near the circle in part (b) and 30 μm above the surface; two ions would lie approximately $L = 4.5\,\mu$m apart with their axis parallel to the electrode axes. The intrinsic asymmetry of the electrodes relative to an ion's position leads to anharmonic perturbations in the trapping potential.

For a single ion in this trap,

$$\begin{pmatrix}\Delta f_1\\ \Delta f_2\\ \Delta f_3\end{pmatrix} = \begin{pmatrix}-2.9 & -2.7 & 0.04\\ -2.7 & -0.9 & 0.2\\ 0.04 & 0.2 & -0.1\end{pmatrix}\begin{pmatrix}n_1\\ n_2\\ n_3\end{pmatrix}\text{Hz}. \tag{31}$$

The largest shifts are a few parts in 10^7 per quantum.

Multi-qubit gates in quantum information processing typically involve multiple ions in the same trap zone. The couplings among the six normal modes of two trapped ions for the trap of figure 7 are

$$\begin{pmatrix}\Delta f_1\\ \Delta f_2\\ \Delta f_3\\ \Delta f_4\\ \Delta f_5\\ \Delta f_6\end{pmatrix} = \begin{pmatrix}-1.4 & -3.2 & -1.3 & -1.6 & 0.03 & 0.03\\ -3.2 & -0.4 & -2.2 & -2.1 & -9.4 & 0.03\\ -1.3 & -2.2 & -0.4 & -1.1 & 0.2 & 0.1\\ -1.6 & -2.1 & -1.1 & 1.6 & -13.5 & 0.3\\ 0.03 & -9.4 & 0.2 & -13.5 & 6.5 & -0.4\\ 0.03 & 0.03 & 0.1 & 0.3 & -0.4 & -0.1\end{pmatrix}\begin{pmatrix}n_1\\ n_2\\ n_3\\ n_4\\ n_5\\ n_6\end{pmatrix}\text{Hz}. \tag{32}$$

The tensor is ordered such that the highest-frequency normal mode is at the top (index 1), and the lowest is 6. Modes 5 and 6 are axial, and modes 1–4 are radial. The modes where the ions' amplitudes have opposite sign (the out-of-phase modes) are 2, 4 and 5, while the in-phase modes are 1, 3 and 6. For comparison, if only the contribution from the Coulomb interaction is included (that is, if the trap potential were perfectly harmonic, having the same single ion trapping frequencies as above), the shifts are

$$\begin{pmatrix}\Delta f_1^c\\ \Delta f_2^c\\ \Delta f_3^c\\ \Delta f_4^c\\ \Delta f_5^c\\ \Delta f_6^c\end{pmatrix}=\begin{pmatrix}0 & 0 & 0 & 0 & 0 & 0\\ 0 & 1.1 & 0 & 0 & -9.4 & 0\\ 0 & 0 & 0 & 0 & 0 & 0\\ 0 & 0 & 0 & 2.2 & -13.7 & 0.1\\ 0 & -9.4 & 0 & -13.7 & 6.7 & -0.1\\ 0 & 0 & 0 & 0.1 & -0.1 & 0\end{pmatrix}\begin{pmatrix}n_1\\ n_2\\ n_3\\ n_4\\ n_5\\ n_6\end{pmatrix}\text{Hz.} \tag{33}$$

On comparing these matrices we observe that in this trap the Coulomb anharmonicity still creates the largest mode-couplings, although some terms arising from the trap potential approach the strength of the Coulomb contribution. However, whereas the Coulomb anharmonicity principally affects only modes of motion where the oscillation of the two ions has a sizeable differential component to the motion, the trap potential anharmonicities couple all modes.

4.3. Coherence during quantum state manipulations

The frequency shifts described in the previous section can become problematic both for motional state engineering [1–4], [10, 25] and in quantum information processing, where the motion of the ions is used in multi-qubit gates. To give an idea of the level at which cross-coupling from anharmonic terms could impede control in typical experiments, we provide two examples: the coherence of a superposition of motional Fock states and loss of fidelity in a two-qubit gate.

Consider the superposition $(|0_Z\rangle+|n_Z\rangle)/\sqrt{2}$ for a mode Z, and assume for simplicity that all other 'spectator' modes can be described by a single Doppler-limit temperature $T_{\rm D}$ [65]. The coherence between the two motional states is given by the off-diagonal element of the density matrix, which evolves in time because of the anharmonic frequency differences. Taking the thermal average of the motional excitation of spectator modes yields

$$\begin{aligned}C(t)=2\left|\rho_{0_Z,n_Z}\right|&=\left|\left\langle \mathrm{e}^{\mathrm{i}2\pi[f_Z(0)-f_Z(n_Z)]t}\right\rangle_{\{n_\alpha\}}\right|\\ &=\left|\prod_{\alpha\neq Z}\left[1-\exp\left(\frac{-hf_\alpha}{k_{\rm B}T_{\rm D}}\right)\right]\left[1-\exp\left(\frac{-hf_\alpha}{k_{\rm B}T_{\rm D}}-\mathrm{i}2\pi\,\chi_{Z\alpha}\,n_Z t\right)\right]^{-1}\right|.\end{aligned} \tag{34}$$

For example, if the superposition is between the ground and first excited states of the highest-frequency radial mode (mode 1) of a single $^{25}\mathrm{Mg}^+$ ion in the surface trap presented in the previous section, and the other two modes are cooled to $T_{\rm D}=0.7\,\mathrm{mK}$, the coherence decays to $1/2$ in 40 ms. Because the cross-couplings are themselves coherent, C recovers to approximately 80% at $1/\chi_{12}\approx 0.4\,\mathrm{s}$ and in principle almost fully recovers at $1/\chi_{13}\approx 25\,\mathrm{s}$. Such recoveries have been observed in other experiments [20]. For a motional superposition with $(|0\rangle+|10\rangle)/\sqrt{2}$, the decay is ten-times faster. Recent experiments in other traps have produced superpositions of motional states with occupations greater than $n=100$, which were manipulated over time scales of milliseconds [10]. If similar experiments were performed in the surface trap described here, the influence of the mode cross-coupling would need to be taken into consideration.

All deterministic multi-qubit gates in trapped-ion quantum information processing rely on transient excitation of motion conditioned on the ions' internal (qubit) states [60, 61, 64, 66, 67]. At present, typical implementations involve cooling the ions to the ground state of one or more modes of motion prior to implementing the gate. To increase the processing speed, it would be advantageous to perform high-fidelity quantum logic gates after only Doppler cooling. This is possible when the ions are well within the Lamb–Dicke regime and such gates have been demonstrated using lasers [68] and magnetic-field gradients [64]. In these cases, all the motional modes are thermally occupied with non-zero $\bar{n}$, and anharmonic effects need to be considered. The gate methods used in these demonstrations are different versions of a common type, which make use of transient motional excitation by an internal-state-dependent force. This force may be applied optically [60, 61, 69] or via microwaves [64, 70], where the form of the state-dependence can be tailored by control of the driving fields.

Here, for simplicity, we consider the approach taken in [61], which assumed a Hamiltonian

$$H = \hbar\Omega(t)\hat{S}_z \cos(\omega t)\eta(\hat{a}\,\mathrm{e}^{-\mathrm{i}\omega_Z t} + \hat{a}^\dagger\,\mathrm{e}^{\mathrm{i}\omega_Z t}), \tag{35}$$

where $\Omega(t)$ is related to the laser fields used to produce the gate, ω is a drive frequency typically near ω_Z, $\hat{S}_z$ is the sum of the Pauli Z operators $|\uparrow\rangle\langle\uparrow| - |\downarrow\rangle\langle\downarrow|$ acting on each ion's spin, $\eta = |\delta k \sigma_1| = |\delta k \sigma_2|$ is the Lamb–Dicke parameter for the interaction between the light fields and the two ions involved in the gate, and $\hat{a}^\dagger$ and $\hat{a}$ are the creation and annihilation operators which act on the mode chosen for the gate. For simplicity, in what follows we assume that $\Omega(t) = \Omega$ for $0 < t < \tau_G$ and is zero otherwise. If $|\Omega|$, $|\omega - \omega_Z| \ll |\omega_Z|$, $|\omega|$ we can make a rotating wave approximation with respect to the motional frequencies, resulting in an evolution operator for the system given by

$$\hat{U}(t) = D(\alpha(t)\hat{S}_z)\exp(\mathrm{i}\Phi(t)\hat{S}_z^2), \tag{36}$$

where $D(\beta)$ is the motional state displacement operator $\exp(\beta\hat{a}^\dagger - \beta^*\hat{a})$ [58], and

$$\alpha(t) = -\frac{\Omega}{\delta}\mathrm{e}^{-\mathrm{i}\delta t/2}\sin(\delta t/2), \tag{37}$$

$$\Phi(t) = \frac{\Omega^2}{4\delta^2}\left[\sin(\delta t) - \delta t\right], \tag{38}$$

with $\delta = \omega - \omega_Z$.

A common method for characterizing the performance of such a gate is to examine the fidelity with which the entangled state $|\psi_{\mathrm{ideal}}\rangle = (|\downarrow\downarrow\rangle - \mathrm{i}|\uparrow\uparrow\rangle)/\sqrt{2}$ is produced from the state $|\downarrow\downarrow\rangle$ when the force pulse is applied in the first half of a spin-echo sequence and $\Omega = \delta$ and $\tau_G = 2\pi/\delta$. Ideally, these values result in $\alpha(\tau_G) = 0$ and $\Phi(\tau_G) = \pi/2$. For general $\alpha(\tau)$, $\Phi(\tau)$, the fidelity for producing $|\psi_{\mathrm{ideal}}\rangle$ at the end of the spin-echo sequence is given by [61]

$$F = |\langle\psi_{\mathrm{ideal}}|\rho|\psi_{\mathrm{ideal}}\rangle| = \tfrac{3}{8} + \tfrac{1}{8}\mathrm{e}^{-2|\alpha(\tau)|^2} + \tfrac{1}{2}\mathrm{e}^{-|\alpha(\tau)|^2/2}\sin[\Phi(\tau)]. \tag{39}$$

In the presence of anharmonicity, errors can enter into this gate in three ways. Firstly, if the motion begins in a distribution of states, each state will have a different mode frequency and therefore a different detuning. Thus, in general the motional state will not return to its initial position at the end of the drive. For a detuning $\delta(1+\epsilon)$ with fractional error $\epsilon \ll 1$, this results in $\alpha(\tau_G) \simeq \pi\epsilon$. The resulting residual entanglement between the internal states and the motion reduces fidelity when the motional degree of freedom is traced out. Secondly, the different detunings cause each initial motional state to enclose a different area of phase space and thus to acquire a different phase. Again using a detuning error parameter ϵ, we find that $\Phi(\tau_G) \simeq (\pi/2)(1-2\epsilon)$. These phases must be averaged over using the distribution of initial motional states. Finally, the transient motional excitation itself will give a time-dependence to the detuning as the excitation increases then decreases during the gate. For the small excitations typical for present multi-qubit operations, this third effect is significantly smaller than the other two, and we ignore it below.

Let us assume that the gate is performed with the duration chosen such that $\tau_G = 2\pi/\delta$ for the detuning corresponding to all modes in the ground state. For ions which start in an incoherent motional state distribution with mean quantum numbers in the set $\{\bar{n}_\alpha\}$, the above expression then leads to a fidelity

$$F = 1 - \frac{3\pi^4}{\delta^2}\left(\sum_{\alpha\neq\beta}\chi_{Z\alpha}\chi_{Z\beta}\bar{n}_\alpha\bar{n}_\beta + \sum_{\alpha=1}^{3N}\chi_{Z\alpha}^2\overline{n_\alpha^2}\right). \tag{40}$$

The bars indicate an average over the incoherent distribution of n. For a thermal distribution, the mean-square n in the last term can be rewritten as $\overline{n_\alpha^2} = \bar{n}_\alpha(2\bar{n}_\alpha + 1)$. Failure of the motional states to return to their original position contributes two-thirds of the infidelity, with the other third due to the distribution of accumulated phases.

Consider two ions in the surface trap described in the previous section, and a two-qubit gate that makes use of the radial rocking mode with frequency $f_2 = 6.8\,\mathrm{MHz}$ (as used in [64]). Implementing such a gate with all modes cooled to the Doppler-limit temperature of $T_\mathrm{D} = 0.7\,\mathrm{mK}$ produces an infidelity of $1 - F = 4\times10^{-2}\ [2\pi(1\,\mathrm{kHz})/\delta]^2$ if all other aspects of the gate are perfect. For multi-qubit gates performed in a similar manner on larger numbers of ions [12, 42], the increased number of motional modes will reduce the fidelity even further. Thus for detunings $\delta > 2\pi(20\,\mathrm{kHz})$, the infidelity is below the level of 10^{-4}, which is often estimated as a requirement for fault-tolerant quantum information processing. Since the cubic terms in the potential scale unfavorably with reduced trap size, anharmonicity may become a significant source of error as traps become smaller. Various approaches may be used to implement a gate in a manner that suppresses these errors. For example, though the detuning in the above example is $\delta = \Omega$, by use of two pulses—one performed in each half of the spin-echo sequence [71]—the detuning could be increased to $\delta = \sqrt{2}\Omega$, thus reducing the error. This approach also has the advantage that the residual displacement arising from errors in detuning can be arranged to be of opposite sign for the two pulses, and hence is canceled out. This is a special case of the more general composite-pulse schemes recently suggested by Hayes *et al* [72], that has been used in gate operations in several experiments [14, 25, 26, 42, 71]. Pulses with non-square shapes may also help in this regard [73]. This method can be extended by increasing the detuning and executing more, but smaller, loops in phase space [74]. At ion–electrode distances of approximately 30 μm, the coherence of motional-state superpositions is currently limited by anomalous heating [75–77], which is larger than the anharmonic infidelity.

5. Sensitivity to electric fields

The range of effects described above focus on problems related to anharmonic trapping potentials. In addition to these, a practical consideration is that anharmonicities introduce a dependence of the secular frequencies on the position of the ion. This means that uniform electric fields can displace the ions and cause the trap frequencies to shift. For the two-layer trap described in section 3.2 and a cubic term with $\lambda_3 = -230\,\mu\text{m}$ (as observed in section 3.3), a field of $2\,\text{V m}^{-1}$ causes a fractional frequency shift of $\simeq 10^{-3}$ (corresponding to 3 kHz in that example). For multiple experiments [14, 25, 26] performed using this trap, we observed that the trap frequency stability of the harmonic trapping potential was better than that of the anharmonic potential. This suggests that frequency instability may have been caused by slow fluctuations in stray electric fields, but this correlation has not been characterized.

6. Conclusion

Anharmonic trapping potentials give rise to a number of effects that should be taken into account when performing quantum state engineering tasks in ion traps. As trap sizes are reduced, these effects become more significant. By building traps with intrinsic geometric symmetry, it should be possible to minimize odd-order anharmonicities. This consideration should be made at the trap design stage. In practice, the fabricated trap is unlikely to be an exact realization of any design. For this purpose, it is desirable to include a sufficient number of independently controllable electrodes to allow anharmonicities to be canceled in situ. In this case, methods such as those given in section 3.5 can be used to null out unwanted terms. In addition to undesirable effects due to strong anharmonic trap potentials, the advent of small traps where these terms can be engineered might also enable novel state-preparation schemes [63] and tunable phase transitions [22, 23].

Acknowledgments

This work was supported by IARPA, NSA, DARPA, ONR and the NIST Quantum Information Program. We thank Christian Ospelkaus for details of the surface-electrode trap and the use of figure 7. We thank John Gaebler and Ulrich Warring for comments on the manuscript. This manuscript is a contribution by the National Institute of Standards and Technology and is not subject to US copyright.

References

[1] Meekhof D M, Monroe C, King B E, Itano W M and Wineland D J 1996 Generation of nonclassical motional states of a trapped atom *Phys. Rev. Lett.* **76** 1796

[2] Monroe C, Meekhof D M, King B E and Wineland D J 1996 A Schrödinger cat superposition state of an atom *Science* **272** 1131

[3] Haljan P C, Brickman K-A, Deslauriers L, Lee P J and Monroe C 2005 Spin-dependent forces on trapped ions for phase-stable quantum gates and motional Schrödinger cat states *Phys. Rev. Lett.* **94** 153602

[4] McDonnell M J, Home J P, Lucas D M, Imreh G, Keitch B C, Szwer D J, Thomas N R, Webster S C, Stacey D N and Steane A M 2007 Long-lived mesoscopic entanglement outside the Lamb–Dicke regime *Phys. Rev. Lett.* **98** 063603

[5] Poschinger U, Walther A, Singer K and Schmidt-Kaler F 2010 Observing the phase space trajectory of an entangled matter wave packet *Phys. Rev. Lett.* **105** 263602

[6] Leibfried D *et al* 2002 Trapped-ion quantum simulator: experimental application to nonlinear interferometers *Phys. Rev. Lett.* **89** 247901

[7] Gerritsma R, Kirchmair G, Zähringer F, Solano E, Blatt R and Roos C F 2010 Quantum simulation of the Dirac equation *Nature* **463** 68–71
[8] Gerritsma R, Lanyon B P, Kirchmair G, Zähringer F, Hempel C, Casanova J, García-Ripoll J J, Solano E, Blatt R and Roos C F 2011 Quantum simulation of the Klein paradox with trapped ions *Phys. Rev. Lett.* **106** 060503
[9] Schmitz H, Matjeschk R, Schneider C, Glueckert J, Enderlein M, Huber T and Schaetz T 2009 Quantum walk of a trapped ion in phase space *Phys. Rev. Lett.* **103** 090504
[10] Zähringer F, Kirchmair G, Gerritsma R, Solano E, Blatt R and Roos C F 2010 Realization of a quantum random walk with one and two trapped ions *Phys. Rev. Lett.* **104** 100503
[11] Blatt R and Wineland D J 2008 Entangled states of trapped atomic ions *Nature* **453** 1008–15
[12] Monz T, Schindler P, Barreiro J T, Chwalla M, Nigg D, Coish W A, Harlander M, Hänsel W, Hennrich M and Blatt R 2011 14-qubit entanglement: creation and coherence *Phys. Rev. Lett.* **106** 130506
[13] Benhelm J, Kirchmair G, Roos C F and Blatt R 2008 Towards fault-tolerant quantum computing with trapped ions *Nat. Phys.* **4** 463–6
[14] Home J P, Hanneke D, Jost J D, Amini J M, Leibfried D and Wineland D J 2009 Complete methods set for scalable ion trap quantum information processing *Science* **325** 1227
[15] Steane A M 2003 Overhead and noise threshold of fault-tolerant quantum error correction *Phys. Rev.* A **68** 042322
[16] Knill E 2005 Quantum computation with realistically noisy devices *Nature* **434** 39–44
[17] Steane A M 1997 The ion trap quantum information processor *Appl. Phys.* B **64** 623–42
[18] James D V F 1998 Quantum dynamics of cold trapped ions with application to quantum computation *Appl. Phys.* B **66** 181–90
[19] Morigi G and Walther H 2001 Two species Coulomb chains for quantum information *Eur. Phys. J.* D **13** 261–9
[20] Roos C F, Monz T, Kim K, Riebe M, Haeffner H, James D F V and Blatt R 2008 Nonlinear coupling of continuous variables at the single quantum level *Phys. Rev.* A **77** 040302
[21] Nie X R, Roos C F and James D F V 2009 Theory of cross phase modulation for the vibrational modes of trap ions *Phys. Lett.* A **373** 422–5
[22] Fishman S, De Chiara G, Calarco T and Morigi G 2008 Structural phase transitions in low-dimensional ion crystals *Phys. Rev.* B **77** 064111
[23] Gong Z-X, Lin G-D and Duan L-M 2010 Temperature-driven structural phase transition for trapped ions and a proposal for its experimental detection *Phys. Rev. Lett.* **105** 265703
[24] Rowe M A *et al* 2002 Transport of quantum states and separation of ions in a dual rf ion trap *Quantum Inf. Comput.* **2** 257
[25] Jost J D, Home J P, Amini J M, Hanneke D, Ozeri R, Langer C, Bollinger J J, Leibfried D and Wineland D J 2009 Entangled mechanical oscillators *Nature* **459** 683–5
[26] Hanneke D, Home J P, Jost J D, Amini J M, Leibfried D and Wineland D J 2010 Realization of a programmable two-qubit quantum processor *Nat. Phys.* **6** 13–6
[27] Lin G-D, Zhu S-L, Islam R, Kim K, Chang M-S, Korenblit S, Monroe C and Duan L-M 2009 Large-scale quantum computation in an anharmonic linear ion trap *Eur. Phys. Lett.* **86** 60004
[28] Steane A 2007 How to build a 300 bit and 1 gigaop quantum computer *Quantum Inf. Comput.* **7** 171
[29] Amini J M, Uys H, Wesenberg J H, Seidelin S, Britton J, Bollinger J J, Leibfried D, Ospelkaus C, VanDevender A P and Wineland D J 2010 Toward scalable ion traps for quantum information processing *New J. Phys.* **12** 033031
[30] Porras D and Cirac J I 2004 Bose–Einstein condensation and strong-correlation behaviour of phonons in ion traps *Phys. Rev. Lett.* **93** 263602
[31] Deng X-L, Porras D and Cirac J I 2008 Quantum phases of interacting phonons in ion traps *Phys. Rev.* A **77** 033403
[32] Brown K R, Ospelkaus C, Colombe Y, Wilson A C, Leibfried D and Wineland D J 2011 Coupled quantized mechanical oscillators *Nature* **471** 196–9

[33] Harlander M, Lechner R, Brownnutt M, Blatt R and Hänsel W 2011 Trapped-ion antennnae for the transmission of quantum information *Nature* **471** 200–3

[34] Tian L, Rabl P, Blatt R and Zoller P 2004 Interfacing quantum-optical and solid-state qubits *Phys. Rev. Lett.* **92** 24

[35] Wineland D J, Monroe C, Itano W M, Leibfried D, King B E and Meekhof D M 1998 Experimental issues in coherent quantum-state manipulation of trapped atomic ions *J. Res. Natl Inst. Stand. Technol.* **103** 259–328

[36] Heinzen D J and Wineland D J 1990 Quantum-limited cooling and detection of radio-frequency oscillations by laser-cooled ions *Phys. Rev.* A **42** 2977–94

[37] Hensinger W K, Utami D W, Goan H-S, Schwab K, Monroe C and Milburn G J 2005 Ion trap transducers for quantum electromechanical oscillators *Phys. Rev.* A **72** 041405

[38] Seidelin S *et al* 2006 Microfabricated surface-electrode ion trap for scalable quantum information processing *Phys. Rev. Lett.* **96** 253003

[39] Leibrandt D R *et al* 2009 Demonstration of a scalable, multiplexed ion trap for quantum information processing *Quantum Inf. Comput.* **9** 901–19

[40] Daniilidis N, Narayanan S, Möller S A, Clark R, Lee T E, Leek P J, Wallraff A, Schulz St, Schmidt-Kaler F and Häffner H 2011 Fabrication and heating rate study of microscopic surface electrode ion traps *New J. Phys.* **13** 013032

[41] Häffner H *et al* 2005 Scalable multiparticle entanglement of trapped ions *Nature* **438** 643

[42] Leibfried D *et al* 2005 Creation of a six-atom Schroedinger cat state *Nature* **438** 639–42

[43] Barreiro J T, Schindler P, Gühne O, Monz T, Chwalla M, Roos C F, Hennrich M and Blatt R 2010 Experimental multiparticle entanglement dynamics induced by decoherence *Nat. Phys.* **6** 943–6

[44] Islam R *et al* 2011 Onset of a quantum phase transition with a trapped ion quantum simulator arXiv:1103.2400v1

[45] Kielpinski D, Meyer V, Rowe M A, Sackett C A, Itano W M, Monroe C and Wineland D J 2001 A decoherence-free quantum memory using trapped ions *Science* **29** 1013–5

[46] Langer C *et al* 2005 Long-lived qubit memory using atomic ions *Phys. Rev. Lett.* **95** 060502

[47] Monz T *et al* 2009 Realization of universal ion-trap quantum computation with decoherence-free qubits *Phys. Rev. Lett.* **103** 200503

[48] Landau L D and Lifshitz E M 1976 *Mechanics* 3rd edn (London: Butterworth-Heinenann)

[49] Shankar R 1997 *The Principles of Quantum Mechanics* (Berlin: Springer)

[50] Home J P and Steane A M 2006 Electric octopole configurations for fast separation of trapped ions *Quantum Inf. Comput.* **6** 289–325

[51] Kielpinski D, King B E, Myatt C J, Sackett C A, Turchette Q A, Itano W M, Monroe C and Wineland D J 2000 Sympathetic cooling of trapped ions for quantum logic *Phys. Rev.* A **61** 032310

[52] Pozrikidis C 2002 *A Practical Guide to Boundary Element Methods with the Software Library BEMLIB* (London: Chapman and Hall)

[53] Wesenberg J H *et al* 2007 Fluorescence during Doppler cooling of a single trapped atom *Phys. Rev.* A **76** 053416

[54] Hume D 2010 Two species ion chains for quantum logic spectroscopy and entanglement generation *PhD Thesis* University of Colorado

[55] Hume D B, Chou C W, Rosenband T and Wineland D J 2009 Preparation of Dicke states in an ion chain *Phys. Rev.* A **80** 052302

[56] Chou C W, Hume D B, Koelemeij J C J, Wineland D J and Rosenband T 2010 Frequency comparison of two high-accuracy Al^+ optical clocks *Phys. Rev. Lett.* **104** 070802

[57] Monroe C, Meekhof D M, King B E, Jefferts S R, Itano W M and Wineland D J 1995 Resolved-sideband Raman cooling of a bound atom to the 3D zero-point energy *Phys. Rev. Lett.* **75** 4011

[58] Haroche S and Raimond J-M 2006 *Exploring the Quantum: Atoms and Cavities and Photons* (Oxford: Oxford University Press)

[59] Ramsey N 1998 *Spectroscopy with Coherent Radiation: Selected Papers of Norman Ramsey with Commentary* (Singapore: World Scientific)

[60] Sørensen A and Mølmer K 1999 Quantum computation with ions in thermal motion *Phys. Rev. Lett.* **82** 1971–4

[61] Leibfried D *et al* 2003 Experimental demonstration of a robust and high-fidelity geometric two ion-qubit phase gate *Nature* **422** 412–5

[62] Ozeri R *et al* 2007 Errors in trapped-ion quantum gates due to spontaneous photon scattering *Phys. Rev.* A **75** 042329

[63] Marquet C, Schmidt-Kaler F and James D F V 2003 Phonon–phonon interactions due to nonlinear effects in a linear ion trap *Appl. Phys.* B **76** 199–208

[64] Ospelkaus C, Warring U, Colombe Y, Brown K R, Amini J M, Leibfried D and Wineland D J 2011 Microwave quantum logic gates for trapped ions arXiv:1104.3573v1

[65] Leibfried D, Blatt R, Monroe C and Wineland D 2003 Quantum dynamics of single trapped ions *Rev. Mod. Phys.* **75** 281–324

[66] Cirac J I and Zoller P 1995 Quantum computations with cold trapped ions *Phys. Rev. Lett.* **74** 4091–4

[67] Garcia-Ripoll J J, Zoller P and Cirac J I 2003 Speed optimized two-qubit gates with laser coherent control techniques for ion trap quantum computing *Phys. Rev. Lett.* **91** 157901

[68] Kirchmair G, Benhelm J, Zähringer F, Gerritsma R, Roos C F and Blatt R 2009 Deterministic entanglement of ions in thermal states of motion *New J. Phys.* **11** 023002

[69] Lee P J, Brickman K-A, Deslauriers L, Haljan P C, Duan L M and Monroe C 2005 Phase control of trap ion quantum gates *J. Opt.* B **7** S371–83

[70] Ospelkaus C, Langer C E, Amini J M, Brown K R, Leibfried D and Wineland D J 2008 Trapped-ion quantum logic gates based on oscillating magnetic fields *Phys. Rev. Lett.* **101** 090502

[71] Home J P, McDonnell M J, Lucas D M, Imreh G, Keitch B C, Szwer D J, Thomas N R, Stacey D N and Steane A M 2006 Entanglement and tomography of ion spin qubits *New J. Phys.* **8** 188

[72] Hayes D, Clark S M, Debnath S, Hucul D, Quraishi Q and Monroe C 2011 Coherent error suppression in spin-dependent force quantum gates arXiv:1104.1347

[73] Leibfried D, Knill E, Ospelkaus C and Wineland D J 2007 Transport quantum logic gates for trapped ions *Phys. Rev.* A **76** 032324

[74] Sørensen A and Mølmer K 2000 Entanglement and quantum computation with ions in thermal motion *Phys. Rev.* A **62** 022311

[75] Turchette Q A *et al* 2000 Heating of trapped ions from the quantum ground state *Phys. Rev.* A **61** 063418

[76] Deslauriers L, Olmschenk S, Stick D, Hensinger W K, Sterk J and Monroe C 2006 Scaling and suppression of anomalous quantum decoherence in ion traps *Phys. Rev. Lett.* **97** 103007

[77] Labaziewicz J, Ge Y, Antohi P, Leibrandt D, Brown K R and Chuang I L 2008 Suppression of heating rates in cryogenic surface-electrode ion traps *Phys. Rev. Lett.* **100** 013001